



Differences in Oxidation Behavior of Conventionally Cast and Additively Manufactured Co-Base Alloy MAR-M-509

T. Galiullin^{1,2} · R. Pillai^{2,3} · W. J. Quadackers² · D. Naumenko²

Received: 14 August 2023 / Revised: 8 September 2023 / Accepted: 10 September 2023
© The Author(s) 2023

Abstract

High-temperature oxidation behavior of conventionally cast and additively manufactured (AM) Co-base alloy MAR-M-509 was compared in the present study. The specimens were exposed in air at 1000 °C and characterized by means of scanning electron microscopy equipped with energy/wavelength dispersive x-ray spectroscopy (EDX/WDX) and electron backscatter diffraction as well as transmission electron microscopy. Substantial differences in the oxidation processes of two alloy versions were observed. Faster oxidation of the cast alloy was mainly induced by (1) oxidation of coarse primary carbides, (2) internal oxidation and nitridation processes and (3) incorporation of other alloy constituents (e.g., Co, Ni, W) into the Cr-oxide scale. AM specimens, in contrast, formed a more homogeneous, thinner and better adherent external oxide scale. The results are discussed in terms of differences in the chemical composition and alloy microstructure, including the grain size distribution in the material and the morphology of the strengthening precipitate phases.

Keywords High-temperature oxidation · Co-base alloys · MAR-M-509 · Additive manufacturing · Selective laser melting

Introduction

Various high-temperature industrial processes require construction materials that possess an optimal balance of mechanical strength, corrosion resistance, manufacturability and repairability. An optimal compromise in material properties to comply with the above-mentioned requirements was found in iron-, nickel- and cobalt-base

✉ T. Galiullin
t.galiullin@fz-juelich.de

¹ Projekttraeger Juelich, Forschungszentrum Juelich GmbH, 52428 Juelich, Germany

² IEK-2, Forschungszentrum Juelich GmbH, 52428 Juelich, Germany

³ Materials Science and Technology Division, Oak Ridge National Laboratory, Oak Ridge, TN 37831-6156, USA

metallic alloys that represent the vast majority of technically used materials at operating temperatures above 600 °C. Apart from relatively high melting temperatures, the success of Fe-, Ni-, Co-base alloys is related to a possibility of extensive alloying, thus providing compositional flexibility and control over the alloy properties. Due to excellent creep and oxidation resistance, some of these alloys are often referred as superalloys and are widely employed in the most demanding applications including high-temperature components of gas turbine engines for aviation and power production.

Although Co-base alloys are not used as widely as Ni-base alloys mainly due to lower creep strength and currently higher price, they are still considered as a competitive alternative in certain applications, predominantly in gas turbine industry. Wrought heat-resistant Co-base alloys such as Haynes 25 and Haynes 188 are typically employed in rather low-stress high-temperature applications requiring good ductility and weldability of the construction materials, in particular in thin-walled parts of combustors, hot gas casings and transition ducts [1]. Compared to solid solution strengthened Ni-base alloys developed for similar applications (e.g., Alloy X and Haynes 230), Co-base alloys often exhibit better creep properties [1, 2] and are claimed to be more resistant against sulfidation attack [3]. However, they may suffer from enhanced oxidation at high temperatures (above 1000 °C) and significant ductility loss during long-term service [4].

Cast Co-base heat-resistant alloys were historically designed as a turbine blade construction material, but were continuously substituted by γ/γ' -Ni-base alloys due to the superior creep strength of the latter materials. Cast Co-base alloys, however, feature a number of attractive properties. The lack of γ/γ' -microstructure and Al results in excellent weldability of this class of alloys that significantly simplifies the repair cycle of the respective components. In addition, cast Co-base alloys typically enter the high-temperature service in as-cast condition [5], since complete solution annealing is not possible due to high thermal stability of carbides. This is contrary to γ' -strengthened Ni-base alloys that undergo complex and expensive multi-step heat-treatment cycles. Furthermore, some cast Co-base alloy grades such as MAR-M-509 exhibit about 1.5 times higher thermal conductivity than Ni-base alloys [6]. This reduces the amount of cooling medium required in the cooled turbine components of the hot section, thereby increasing the engine efficiency. Due to above-mentioned properties cast, Co-base alloys are used in modern gas turbine engines as a material for high-pressure vanes and inlet nozzles and in turbine blades of smaller industrial gas turbines [7].

Oxidation Behavior of Co-base Alloys

In contrast to Fe–Ni and Ni-based materials, only limited data are available in literature on oxidation behavior of commercial Co-base grades with analysis of oxidation performance being often limited to a qualitative comparison to other alloy groups (see, e.g., [8]). However, considerable research was conducted on binary and ternary model Co–Cr alloys. Numerous studies on binary Co–Cr alloys showed that, compared to Ni–Cr, a higher Cr content in the Co-matrix is required for its selective

oxidation and scaling of slow-growing protective Cr_2O_3 [9–11]. In fact, formation of less stable Co-containing oxides was reported also in alloys with high amounts of Cr (25–30 wt%) [10, 12, 13]. Such significant differences in oxidation behavior between Co–Cr and Ni–Cr alloys are related to a high growth rate of transient oxides, mainly CoO and CoCr_2O_4 , that easily overgrow initial Cr_2O_3 nuclei during transient oxidation [11, 14, 15]. The situation is even less favorable due to nearly an order of magnitude slower Cr diffusion in Co-FCC matrix (at 1000 °C) than in Ni [16]. As a result, at the initial stages of exposure, Co–Cr alloys may exhibit a rapid Cr depletion in the subsurface zone with a subsequent breakdown of the protective scale. This makes maintaining chromia growth challenging for the material and limits its maximum service temperature. In low $p\text{O}_2$ environments, where CoO is not thermodynamically stable, the oxidation kinetics of Cr-rich Co–Cr alloys might be virtually similar to Ni–Cr, as was shown by Wood et al. [11].

Additively Manufactured Alloys for High-Temperature Applications

The substantially better weldability of cast Co-base alloys compared to γ' strengthened Ni-base alloys may be particularly beneficial for additive manufacturing (AM) the use of which is currently being extended to high-temperature gas turbine parts [17]. AM techniques such as Electron Beam Melting (EBM) and Selective Laser Melting (SLM) may contribute to an improved design of future high-temperature gas turbine components and simplify their repair cycles [18]. Due to the nature of the additive manufacturing processes, the microstructure of the AM alloys differs substantially from the conventionally manufactured grades despite nearly identical alloy chemistry [17, 19, 20]. The alloy microstructure imparted by the manufacturing was observed to have a strong effect on high-temperature mechanical properties [21, 22] as well as oxidation behavior [23–26] of the AM materials.

The present study focuses on the high-temperature oxidation resistance of two versions of the Co-base alloy MAR-M-509 typically employed in high-temperature stator vanes and turbine blades of aeroengines and industrial gas turbines: conventionally cast by vacuum investment casting and additively manufactured (AM), produced by Selective Laser Melting. The oxidation behavior of alloy specimens was studied in a series of isothermal and discontinuous air exposures at 1000 °C. The differences in oxide morphology between the conventional and AM alloy versions are discussed in the following sections in terms of the alloy microstructure, including the grain distribution in the material and morphology of the strengthening precipitate phases.

Experimental Procedures

Investigated Materials and Chemical Analysis

Commercial conventionally cast MAR-M-509 was supplied by Doncasters Precision Castings Bochum GmbH in the as-cast condition in form of a cylindrical rod

measuring 25 mm in diameter. A square $12 \times 12 \text{ mm}^2$ rod of AM MAR-M-509 produced by Selective Laser Melting was provided by MAN Energy Solutions in the as-built condition.

The chemical compositions of the alloy batches investigated in the present study were obtained by inductively coupled plasma-optical emission spectroscopy (ICP-OES) and combustion analysis and are listed in Table 1. The alloy MAR-M-509 is based on the Co–Cr–Ni–W system and contains a relatively high C content (0.6 wt. %). High-temperature mechanical strength of the alloy is provided by extensive precipitation of (Ta, Ti, Zr)-rich and Cr-rich carbides together with solid solution strengthening mainly by W [5]. A Ni addition of approximately 10% is required to stabilize the Co-FCC structure, while a high Cr level (23 wt. %) ensures the formation of a protective Cr_2O_3 layer on the alloy surface thus providing long-term oxidation resistance. The measured compositions of the cast and AM versions of MAR-M-509 were similar with minor differences in concentrations of main alloying elements such as Cr, Ni, W and Ta. Although not included in the nominal composition of MAR-M-509, Al additions were found in both alloys studied. A higher Al content was measured in the cast alloy.

Specimens measuring $20 \text{ mm} \times 10 \text{ mm} \times 1 \text{ mm}$ were cut from the delivered rods by spark erosion and subsequently ground to 1200-grit surface finish using SiC grinding papers. The AM samples were sectioned perpendicular to the build direction (transversal cut). All test coupons were ultrasonically cleaned with ethanol prior to exposure.

High-Temperature Exposures

Isothermal and discontinuous high-temperature exposures were carried out in a horizontal resistance-heated tube furnace at $1000 \text{ }^\circ\text{C}$ for up to 1000 h in dry laboratory air. Specimens were hung using alumina rods on an alumina specimen holder that was moved in the furnace, once the desired temperature of the heated zone was reached. Selected discontinuous exposures were carried out using single alumina crucibles for each specimen to evaluate the spallation behavior of the alloys by measuring the weight of spalled oxide. Specimens were removed every 48 h, cooled down to room temperature, weighed and visually examined.

A SETARAM TGA 92 thermobalance was employed to obtain continuous weight change data at $1000 \text{ }^\circ\text{C}$ for up to 72 h in synthetic air. The specimens were heated inside the TG furnace at a rate of $90 \text{ }^\circ\text{C}/\text{min}$ and upon reaching the desired exposure

Table 1 Chemical compositions of investigated cast and additively manufactured Co-base alloy MAR-M-509 determined by ICP-OES and combustion analysis (IR)

	Co	Cr	Ni	W	Ta	Ti	Zr	Al	C	O	N	S	
Cast	wt%	Bal.	22.70	10.10	6.94	3.32	0.371	0.314	0.628	0.630	0.0021	0.0010	0.0040
	at%	Bal.	25.91	10.21	2.24	1.09	0.460	0.204	1.381	3.113	0.0078	0.0042	0.0074
AM	wt%	Bal.	22.90	10.00	7.15	3.58	0.233	0.480	0.141	0.540	0.0067	0.0089	0.0027
	at%	Bal.	26.49	10.25	2.34	1.19	0.293	0.316	0.314	2.704	0.0231	0.0383	0.0048

time cooled down at 10 °C/min. The volume flow rate of the gas was maintained at 2 l/h at a total pressure of 1 bar.

Characterization of the Oxidized Specimens

Phase compositions of the oxide scale of the selected specimens were analyzed by Empyrean X-Ray Diffractometer of Malvern Panalytical. The set-up was equipped with a Cu cathode (40 kV/40 mA) and operated in the parafocusing Bragg–Brentano geometry with the scanning step of 0.026° per 1 s and 0.4° divergence.

Metallographic cross sections of the samples for subsequent microscopical studies were prepared in conventional way including (1) sputtering of a thin gold layer on the sample surface, (2) electroplating of a 10–20 µm thick Ni-layer, (3) mounting of the sample in an epoxy resin and (4) grinding of the mounted samples with SiC papers down to 1200 grit surface finish followed by a series of polishing steps with diamond pastes down to 1 µm surface finish. The final polishing step was performed in a SiO₂ colloidal slurry. The plane of the cross-section was aligned perpendicular to the wide surface of the sample.

Scanning electron microscopy (SEM) studies were carried out using two SEM systems of Zeiss: (1) SUPRA 50 VP coupled with a X-Max energy dispersive X-ray (EDX) detector (Oxford Instruments) and (2) Merlin with a mounted Nordlys Electron backscattered diffraction (EBSD) system (Oxford Instruments).

Selected specimens were analyzed in a Zeiss Libra 200 transmission electron microscope (TEM) with an accelerating voltage of 200 kV and equipped with X-Max 80 EDX (Oxford Instruments). Lamellas for TEM measuring 10 × 10 × 0.1 µm³ were prepared in a Auriga cross beam SEM with focused ion beam (FIB) using a Ga-ion source.

Results

Microstructure in As-received Condition

The back scattered electron (BSE) images in Fig. 1 show the microstructure of the as-received cast and AM alloy MAR-M-509. The microstructure of the cast MAR-M-509 was in agreement with the data reported in literature [27, 28] and could be characterized by carbide rich eutectic regions in the Co-matrix. A coupled SEM–EBSD–EDX analysis (Fig. 2a) revealed two types of carbide phases: (Ta, Ti, Zr)-rich MC carbides (large network of blocky precipitates appearing white in the BSE images in Fig. 1a) and Cr-rich M₇C₃ often present as an eutectic structure with the Co-FCC matrix. Figure 1b reveals a completely different microstructure of the AM material compared to the conventional alloy (note that the BSE-image of the AM alloy was obtained at much higher magnification). Alloy grains could be clearly distinguished in the BSE image by small Ta-rich MC-type carbides (~0.5 µm in diameter) along the grain boundaries and very fine precipitates of the same type within the grains. The alloy grain structure was

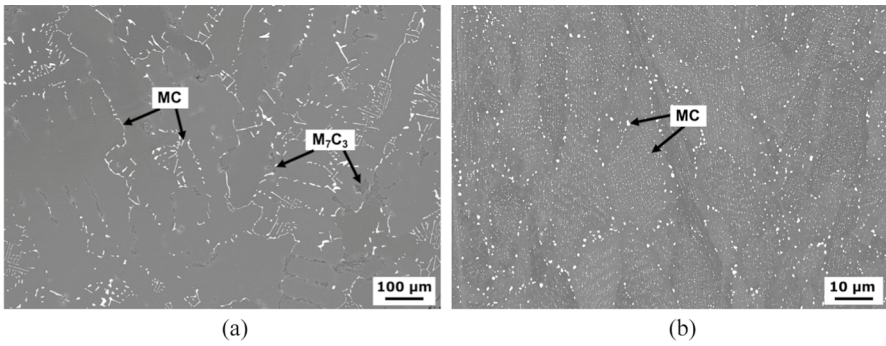


Fig. 1 Microstructure of the as-received **a** cast and **b** AM MAR-M-509. Note the much higher magnification in **(b)**

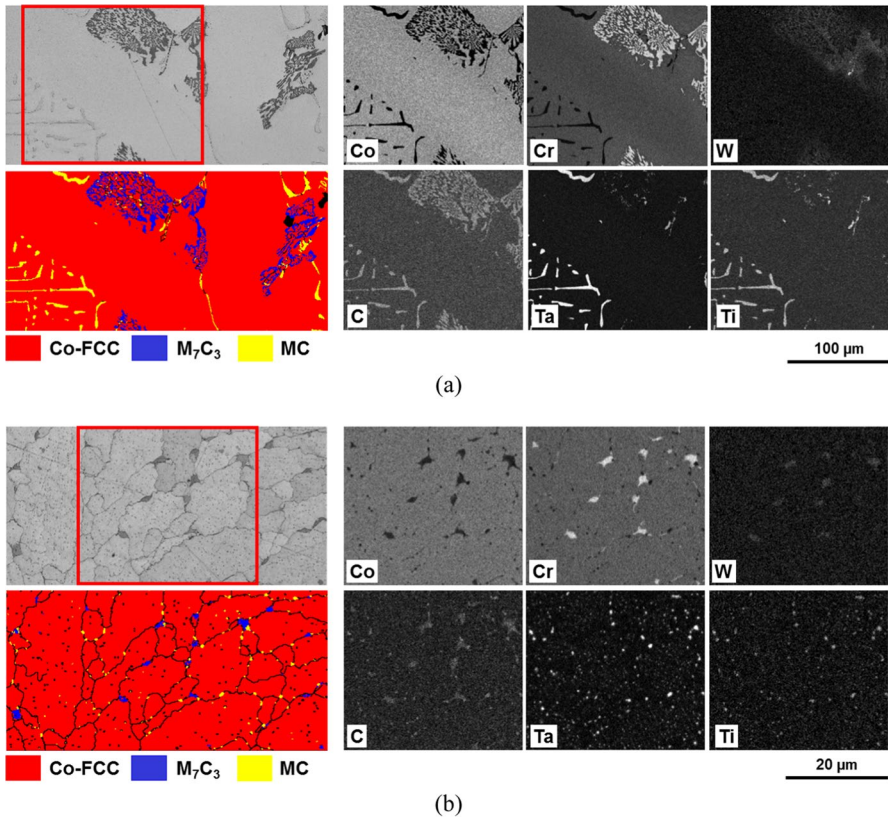


Fig. 2 EBSD band contrast image and phase color map with corresponding EDX element maps from **a** cast and **b** AM MAR-M-509 (transverse cross-section, perpendicular to the build direction) in as-received state. In the EBSD phase map red corresponds to the Co-FCC matrix, blue to M_7C_3 and yellow to MC. Note the much higher magnification in **(b)** compared to **(a)**

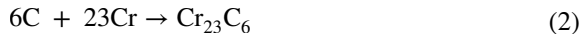
inhomogeneous with grain morphology varying from small equiaxed (<5 μm) to relatively large columnar (40–100 μm). Formation of elongated grains was more pronounced along the build direction. In addition, the microstructure of the AM alloy featured Cr-rich M_7C_3 precipitates that were nearly exclusively found at the grain-boundaries and were generally larger (1–2 μm) than the MC precipitates (Fig. 2b).

High-Temperature Exposures in Air

Phase Equilibria at 1000 °C

During long-term exposures at 1000 °C in the present study, MAR-M-509 specimens underwent thermally induced phase changes in the microstructure that is mainly related to decomposition of primary carbides and formation of secondary precipitate phases, in agreement with [27]. Undesired topologically close packed phases (TCP) such as σ , μ and Laves, often observed in carbide-strengthened Co-base alloys after long-term exposures at temperatures below 900 °C [5], were not found in the present study.

During aging the eutectic $\text{M}_7\text{C}_3 + \gamma\text{-Co}$ structures exhibited a decomposition of M_7C_3 to (Cr, W)-rich M_{23}C_6 . The carbide transformation was accompanied by the release of C to the alloy matrix promoting precipitation of the fine secondary M_{23}C_6 [5]. The phase transformations could be described by the following reactions [5, 29]:



Another microstructural feature observed during exposure at 1000 °C was the formation of the Cr-rich M_{23}C_6 at the surface of the primary MC carbides. The effect likely occurred through partial decomposition of the MC carbides during aging [5, 27, 30]. In addition, very fine secondary (Ta, Ti, Zr)-rich precipitates were found in the alloy matrix although they could not be unequivocally identified by EBSD due to their small size. These precipitates were likely MC-type carbides based on the EDX analysis.

Similar to the cast alloy, transformation of primary M_7C_3 carbides to M_{23}C_6 was observed in the AM specimens. Isothermal exposure also resulted in coarsening of both M_{23}C_6 and MC precipitates along the grain-boundaries. No other phases were detected in the microstructure.

Isothermal Oxidation

Figure 3 shows thermogravimetric data for cast and AM MAR-M-509 specimens obtained during isothermal air exposures at 1000 °C. The cast version showed a nearly two times higher weight gain after 72 h of exposure (Fig. 3a) with about one order of magnitude higher instantaneous apparent parabolic rate constant (Fig. 3b).

In contrast, the AM specimens showed a substantially lower weight gain, which is comparable to that of the wrought Co-base alloys Haynes 25 and Haynes 188.

The cross-sections of oxide scales formed on cast and AM MAR-M-509 after 72 h at 1000 °C in air are shown in Fig. 4. Chromia, as expected, was the main oxidation product in both studied materials. The oxidation behavior of the conventional MAR-M-509 (Fig. 4a, c) was, however, significantly affected by the presence of large primary carbides (mainly of MC-type) that oxidized rapidly when located at the specimen surface or in the subsurface region. The process was characterized by decomposition of the carbides into (Ti, Ta)-oxides that were overgrown by Cr_2O_3 and (Co, Ni, Cr)-rich spinel. Such surface regions showed a very inhomogeneous scale structure with high amounts of cracks and pores. A nearly continuous thin (Co, Ni) Cr_2O_4 spinel layer was observed above chromia in the surface areas not directly affected by the oxidized carbides, as depicted in Fig. 4c.

Fine (Ta, Ti)-rich oxide particles were further found at the scale-alloy interface. The precipitates most likely resulted from the minor concentrations of Ta and Ti available in the Co-matrix as well as Ta/Ti-supply from the decomposed MC carbides. Moreover, the cast alloy suffered from internal oxidation and nitridation processes characterized by precipitation of rather equiaxed Al_2O_3 and needle-shaped AlN beneath it.

In contrast to the cast alloy, AM MAR-M-509 formed a relatively homogeneous Cr_2O_3 scale along the whole specimen surface (Fig. 4b, d). Due to the fundamentally different microstructure of the AM alloy with fine carbide precipitates, the direct oxidation of (Ti, Ta)-rich MC carbides was not observed, although it might occur during the very early stages of oxidation. Instead, the alloy exhibited formation of internal (Ti, Ta)-oxides that propagated toward the alloy bulk preferentially along the grain boundaries. The depth of the internal oxidation zone was not uniform likely due to the inhomogeneous grain distribution in the alloy (compare with Fig. 2b). Similar to the cast MAR-M-509, the internal oxidation was

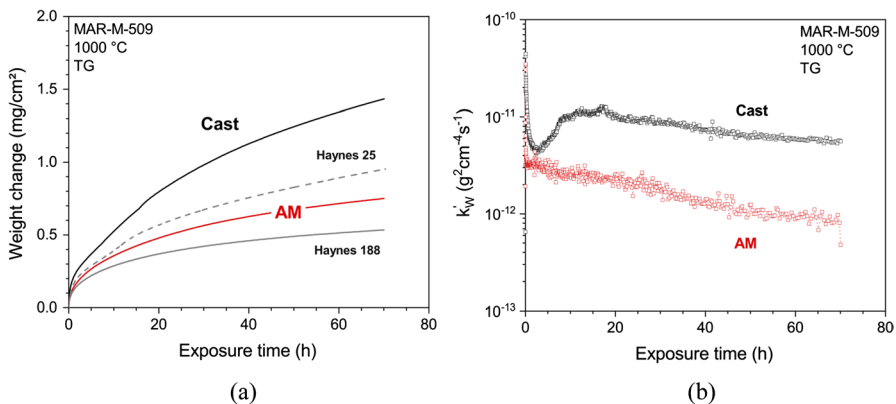


Fig. 3 **a** Weight change and **b** calculated instantaneous apparent parabolic rate constants [34] during isothermal exposure of cast and AM MAR-M-509 at 1000 °C in synthetic air. Data for wrought Co-base alloys was obtained at similar exposure conditions and is shown here as a reference (unpublished results)

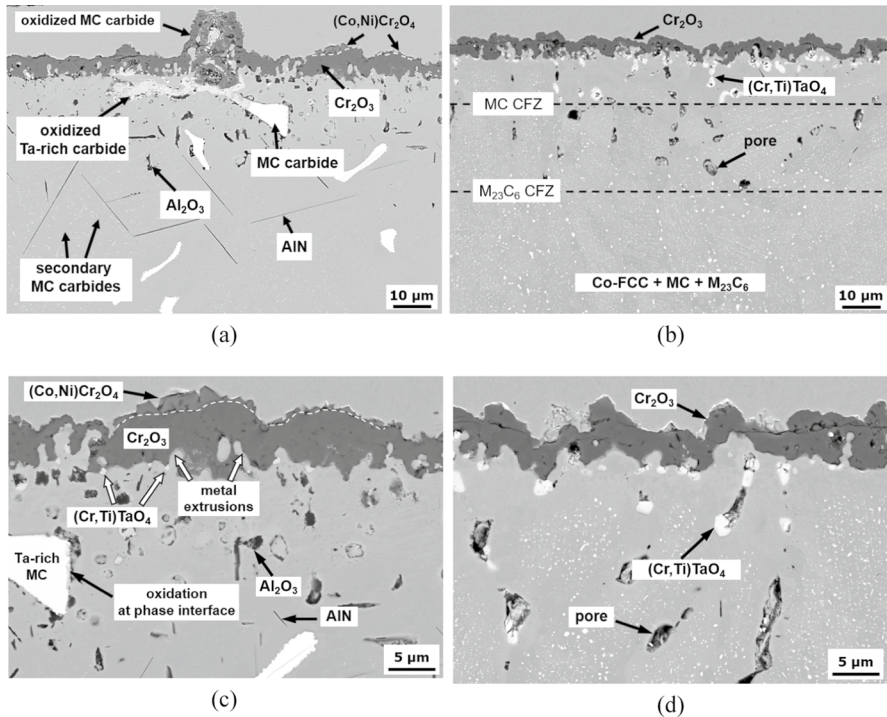


Fig. 4 BSE images of cross-sectioned **a, c** cast and **b, d** AM MAR-M-509 after isothermal exposure (TG) for 72 h at 1000 °C in synthetic air. Although not shown in the image, some minor, fine Al_2O_3 particles were observed in the AM specimen

accompanied by local volume increase resulting in formation of matrix extrusions into the oxide scale and local cracking of the chromia (Fig. 4b). In addition to internal (Ta, Ti)-oxides, minor Al_2O_3 precipitates were also found.

The internal oxidation zone advanced at the expense of MC carbides that supplied Ta and Ti for internal oxide formation resulting in development of a carbide free zone (MC CFZ). The dissolution of the fine carbide precipitates initiated mainly at the grain boundaries followed by the precipitates within the alloy grains, as can be seen in BSE image in Fig. 4b. In addition, EDX element maps taken from the subsurface region (not shown here) revealed decomposition of the grain boundary Cr-rich carbides due to Cr consumption for oxide formation. Due to higher Cr consumption and/or its faster diffusion than Ta, the CFZ corresponding to M_{23}C_6 was more pronounced and uniform than the MC CFZ, $31.2 \pm 2.1 \mu\text{m}$ and $17.2 \pm 9.2 \mu\text{m}$, respectively. Dissolution of MC and especially relatively coarse M_{23}C_6 at the grain boundaries led to formation of pores in the subsurface region. Oxidation-induced dissolution of Cr-rich carbides also took place in the cast alloy; however, the carbide free zone was not clearly visible after 72 h of exposure likely due to the large size of the precipitates. The M_{23}C_6 CFZ was

however observed after longer exposure times (as will be discussed in the following section).

The observed (Ti, Ta)-rich oxide phase, formed either by in situ oxidation of coarse primary MC carbides in cast MAR-M-509 or as internal oxides in the AM alloy, was identified by XRD as the rutile-type TiTaO_4 . EDX point analysis of these oxide precipitates also revealed solubility of Cr. Taking into account very similar lattice parameters of TiTaO_4 and CrTaO_4 [31–33], the formation of a solid solution of both phases is likely.

Long-term Discontinuous Exposures

Figure 5 depicts the weight change data obtained during discontinuous air exposures at 1000 °C. Cast MAR-M-509 exhibited an extensive oxide scale spallation starting already after the third cycle at 1000 °C. After approximately 100 h, the total weight change curve for the cast alloy indicated nearly linear oxidation kinetics with a weight uptake of almost 6 mg/cm² after 1000 h. First indications of breakaway oxidation were observed at the specimen edges, that was associated with the rapid formation of outward growing (Co, Ni)-rich oxides (not shown here). In contrast, the AM specimens showed a substantially lower oxidation rate with only minor scale spallation.

Discontinuous exposure of cast MAR-M-509 for longer times (1000 h) resulted in complex microstructural changes induced by oxidation, as depicted in the BSE images in Fig. 6a, c. Extended cracks could be observed in the scale, in particular, in the areas of enhanced oxidation adjacent to the primary carbides. Compared to the short-term isothermal exposures discussed above, the incorporation of Co into the

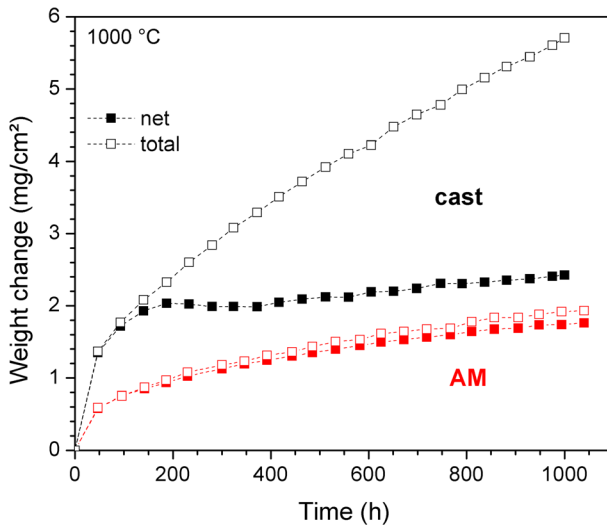


Fig. 5 Total and specimen weight changes of cast and AM MAR-M-509 during discontinuous exposure in laboratory air at 1000 °C (measured every 48 h). The total weight change includes the amount of spalled oxide collected in the crucible

scale was more pronounced in the areas not affected by the carbide oxidation. The surface of the oxidized specimens was green in color typical for the Cr-rich (Co, Ni, Cr)-spinel [35]. Furthermore, continuous Cr loss in the subsurface region to maintain protective oxide scaling led to dissolution of Cr-rich $M_{23}C_6$ carbides.

The long-term exposures of the cast alloy resulted in rapid propagation of the internal oxidation (IOZ) and nitridation zones (INZ). After 300 h at 1000 °C, the IOZ and INZ widths were reaching $68.4 \pm 6.3 \mu\text{m}$ and $192.1 \pm 26.8 \mu\text{m}$, respectively. After exposure for 1000 h AlN precipitates were even found in the specimen center (i.e., at a depth of 500 μm). The morphology of internal Al_2O_3 precipitates changed from a rather globular in the vicinity of the external oxide scale to an acicular (needle or platelet) shape nearer to the interface between IOZ and INZ.

The oxide scale microstructure of AM MAR-M-509 after discontinuous air exposure for 1000 h at 1000 °C is presented in the BSE image in Fig. 6b, d. Compared to the short-term isothermal exposures the oxide scale featured local formation of outer (Co, Ni) Cr_2O_4 spinel, typically next to the cracks in the external scale. In addition, internal oxide precipitates exhibited substantial coarsening during the course of exposure that resulted in an increased number of the matrix extrusions into the outer scale. Propagation of IOZ and CFZ corresponding to $M_{23}C_6$ and MC followed approximately parabolic growth kinetics with the local grain boundary distribution having a strong effect on the width of each zone. A more uniform CFZ (MC-type carbides) was established after longer exposure times, as dissolution of Ta-rich MC

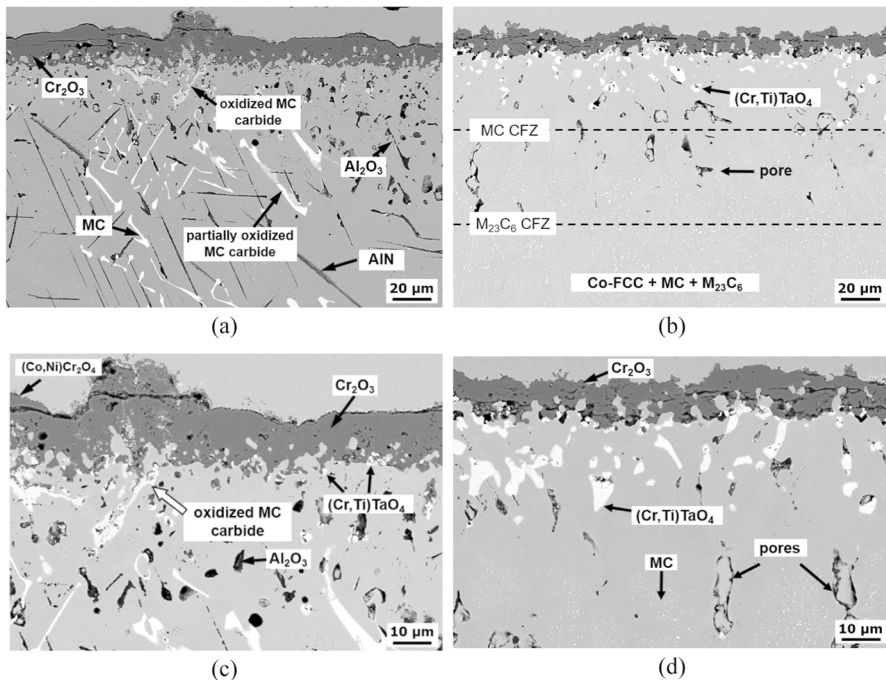


Fig. 6 BSE images of cross-sectioned **a, c** cast and **b, d** AM MAR-M-509 after discontinuous exposure for 1000 h at 1000 °C in air

carbides extended to the intragranular precipitates. The growth rate of the CFZ corresponding to $M_{23}C_6$ was about four times higher compared to the CFZ related to MC precipitates.

Cr concentrations measured by EDX in the alloy matrix after isothermal and discontinuous air exposures at 1000 °C are compared in Fig. 7. The concentration profiles in cast MAR-M-509 were steep with pronounced Cr depletion observed in the subscale zone, whereas the AM alloy maintained relatively high Cr levels at the alloy-oxide interface even after longer exposure times. The distinctive peak in the EDX concentration profiles corresponded approximately to the boundary of $M_{23}C_6$ carbide free zone and was a result of oxidation-induced carbide dissolution and back diffusion of C [36, 37].

Post-exposure microstructural analysis also revealed substantial differences in chromia growth rates between the two alloy versions. Comparison of the scales formed on cast and AM MAR-M-509 (Fig. 6) clearly reveals a thicker Cr_2O_3 layer on the conventionally manufactured alloy. Scale thicknesses measured after isothermal and discontinuous exposures at 1000 °C are plotted in Fig. 8 (avoiding local areas of oxidized primary carbides in the cast alloy). Although the measured values showed considerable scatter, the data could be fitted reasonably well by a classic parabolic time dependence. The parabolic rate constants for cast and AM MAR-M-509 were determined as $k_p^{Cast} = 2.1 \times 10^{-17} \text{ m}^2 \text{ s}^{-1}$ and $k_p^{AM} = 9.9 \times 10^{-18} \text{ m}^2 \text{ s}^{-1}$, respectively.

The role of primary carbides on oxidation performance of the cast alloy, differences in internal oxidation (nitridation) processes between the conventional and AM MAR-M-509 and possible reasons for the faster chromia scaling on the cast alloy will be addressed in the following sections.

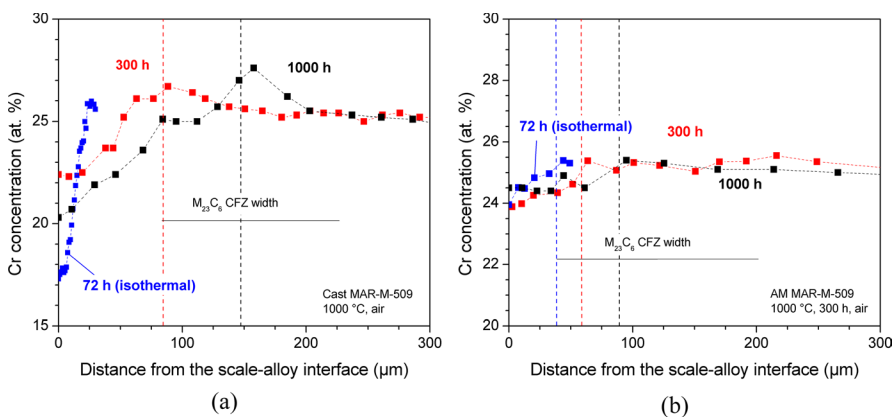


Fig. 7 Cr concentration profiles for **a** cast and **b** AM MAR-M-509 measured by EDX in the alloy matrix after isothermal exposure for 72 h in synthetic air and discontinuous exposures for 300 h and 1000 h in air at 1000 °C. The values for the cast alloy were obtained in the areas located far from the oxidized primary carbides. The dashed lines indicate average $M_{23}C_6$ CFZ widths measured by image analysis

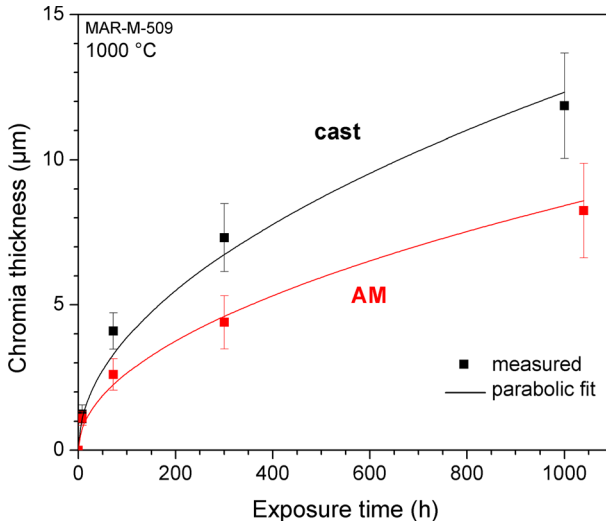


Fig. 8 Evolution of Cr_2O_3 scale on cast (in the areas far from oxidized primary carbides) and AM MAR-M-509 during exposure at 1000 °C as measured by image analysis of cross-sectioned specimens

Discussion

Oxidation of Primary Carbide Precipitates in Cast MAR-M-509

High-temperature oxidation of carbide precipitates located near the sample surface is commonly observed in metallic materials with developed network of primary (interdendritic) carbides, typically in cast austenitic alloys. Reger and Remy [38] studied the high-temperature low cycle fatigue behavior of Ni-base superalloy IN100 and observed oxidation of coarse Ti-rich MC carbides present in the microstructure. Oxidized precipitates acted as initiation sites for fatigue crack development, significantly affecting performance of the material. An even stronger effect of in situ carbide oxidation on the material lifetime under cyclic mechanical load was reported by Reuchet and Remy [39] for the Co-base alloy MAR-M-509. The authors found a substantial decrease in fatigue life at 900 °C in air compared to exposures in vacuum, which was correlated with oxidation of Ta-rich MC precipitates. Pronounced oxidation of interdendritic Cr-rich M_{23}C_6 carbides during high-temperature exposure of high C cast heat-resisting Fe–Ni–Cr alloys was reported in numerous investigations, but analyzed in detail by Belen et al. [40] and Becker et al. [41]. Oxidation of carbides was accompanied by a local volume increase and proceeded at high rates that depended more on the precipitates distribution (e.g., size, shape) rather than detailed alloy composition [41]. Rapid propagation of the oxidation front was attributed to the preferential oxygen transport along the oxidized carbide-alloy matrix interfaces. The effect was qualitatively similar to the enhanced internal oxidation of Al observed in Ni-base alloys [42, 43], where phase interfaces between the elongated rod-shaped Al_2O_3 precipitates and alloy matrix promoted oxygen diffusion.

Oxidation of primary (Ta, Ti)-rich carbides in cast MAR-M-509 observed in the present study showed strong local variation due to the irregular precipitate morphology. Although the oxidation occurred locally, only when MC particles were present at (or near) the surface, it had a tremendous effect on the overall oxidation behavior of the alloy. Thick oxide nodules at the surface could be found at least every 100 μm in the cross-sections of exposed specimens.

The initial reaction of the carbides proceeded at high rates with formation of thick oxide nodules of mixed composition $(\text{Cr,Ti})\text{TaO}_4 + \text{Cr}_2\text{O}_3 + (\text{Co, Ni, Cr})\text{-spinel}$ (Fig. 4a). In the case of coarse MC precipitates, as the carbide oxidation front propagated further (to the alloy interior), the reaction became more homogeneous resulting mainly in formation of internal $(\text{Cr, Ti})\text{TaO}_4$. Depending on the actual orientation of the MC precipitates and their size (Fig. 1a), internal oxidation could locally advance deeper toward the alloy bulk. Another important feature of the data in Fig. 4a was presence of internal alumina particles at the carbide-alloy interface, also in the areas where the precipitate had not yet reacted, indicating enhanced oxygen diffusion along the phase interfaces [41, 42]. In fact, a thin layer of $(\text{Cr, Ti})\text{TaO}_4$ was found at the precipitate surface in the unreacted part of the MC carbide in Fig. 4c resulting from enhanced oxygen transport along the carbide-alloy phase interface. Similar observations were made in the cast MAR-M-509 specimens after longer exposure times, where a number of oxidized MC carbides were found deeper in the alloy, as indicated in the BSE image after 1000 h at 1000 °C [44] in Fig. 6a. The MC carbide was cut through by a needle-shaped Al_2O_3 that supplied oxygen along the internal oxide-matrix interface for the carbide decomposition.

Poor scale adherence in cast MAR-M-509 was mainly induced by the oxidation of primary carbides leading to formation of large areas of inhomogeneous mixed oxide scale with microstructural defects (cracks, pores) and matrix extrusions caused by local volume expansion. Formation of cracks across the thick oxide nodules and affected areas (Figs. 4a and 6a) upon thermal cycling led to pronounced scale spallation.

Internal Oxidation and Nitridation Processes

Cast and AM MAR-M-509 in the present study exhibited essentially distinct types of internal oxidation processes and their kinetics. The AM alloy showed formation of internal $(\text{Cr, Ti})\text{TaO}_4$ with minor amounts of Al_2O_3 . The conventional alloy, in contrast, featured pronounced internal oxidation and nitridation of Al, while precipitation of Ta-rich oxides, apart from decomposition of coarse MC carbides discussed above, was limited to the scale-alloy interface. While more pronounced internal oxidation of Al in the cast alloy was directly related to the higher Al concentration in the alloy matrix, the internal nitridation processes and internal oxidation of Ta were significantly affected by the alloy microstructure.

Internal Nitridation of Al

Chemical degradation of metallic materials during high-temperature exposures in air is generally dominated by oxidation; however, the presence of relatively high amounts of nitrogen in the environment may lead to internal nitridation attack [45]. Similar to the internal oxidation, the nitriding reaction is possible due to solubility of nitrogen in the common high-temperature austenitic alloys Fe-, Ni- and Co-base alloys together with its relatively high diffusion coefficient. Prerequisite for internal nitridation to occur under predominantly oxidizing conditions is often related to the development of microstructural defects (cracks, pores) in the external chromia or alumina scale and/or its spallation during long-term and/or cyclic exposure [46]. It results in the direct access of nitrogen to the base metal, its dissociation at the metallic surface and subsequent penetration into the alloy bulk. Transport of nitrogen to the metal surface was also claimed to result from permeability of chromia to atomic nitrogen [47–49]. Local supersaturation of nitrogen in the alloy matrix and presence of the nitride-forming alloying elements leads to precipitation of internal nitrides, most commonly TiN [50, 51], AlN [51–53] or less thermodynamically stable Cr₂N [52, 53].

Internal nitridation during long-term air exposure of cast MAR-M-509 in the present study was significant (Fig. 6a) and accompanied by needle-shaped AlN formation. Permeation of nitrogen to the metal surface was likely related to a very inhomogeneous oxide scale with a large number of microstructural defects. Formation of pores and cracks caused by in situ oxidation of carbides could result in a molecular transport of nitrogen through the oxide scale to the alloy surface. Further combined oxidation and nitridation reaction can be understood using the treatment of Meijering [54] for internal corrosion by two different oxidants. According to the analysis, thermodynamically more stable internal Al₂O₃ forms in the subsurface region [52], while less stable AlN can only precipitate beneath the internal oxidation zone. Relatively high levels of nitrogen are maintained within the IOZ, because in these regions the Al in the remaining alloy matrix is virtually completely depleted [44, 55, 56]. At the internal oxidation front, where the oxygen content is low, high nitrogen permeability favors precipitation of AlN.

The INZ growth in cast MAR-M-509 was rapid with the formation of needle-shaped AlN precipitates. No other nitride phases (e.g., TiN or Cr₂N) were found. Upon extended high-temperature exposure both IOZ and INZ expanded according to parabolic and nearly linear kinetics, respectively. The estimation of the INZ growth kinetics was, however, somewhat problematic due to considerable scatter of the data after short-term exposures and extension of the nitridation to the specimen core after long-term tests (Fig. 6a). Propagation of the IOZ proceeded, on the one hand, by in situ conversion of AlN precipitates into Al₂O₃ at the IOZ/INZ interface [54], according to displacement reaction



The released nitrogen by the reaction 3 diffused toward the specimen center to support propagation of the INZ. Continuous transformation of internal nitrides to

oxides was evident in the EDX element maps (not shown here) depicting needle-shaped Al_2O_3 in the inner part of the IOZ. In addition, the advancement of the IOZ was accompanied by a nucleation of new oxide precipitates that formed by the reaction of incoming oxygen and Al available in the INZ [57].

In contrast to the conventional cast alloy, internal nitridation was not observed in AM MAR-M-509 due to.

- Very low Al content (Table 1) and consequently its low activity in the alloy matrix. In fact, even formation of internal Al_2O_3 was limited and only minor precipitates were found,
- More dense and adherent external chromia scale that could hinder nitrogen access to the metal surface.

Formation of Internal (Cr, Ti)TaO₄

Formation of the rutile-type Ta, Ti-rich oxides was previously shown by Jalowicka et al. [58] during high-temperature oxidation of single-crystal Ni-base superalloy PWA1483 and later by Nowak et al. [59] in the polycrystalline Ni-base alloy IN792. The authors observed the oxide phase TiTaO_4 beneath the external chromia scale, indicating its higher thermodynamic stability. In the same study of Jalowicka et al. [58], CrTaO_4 and TiTaO_4 were also found for the Ni–Cr–Al model alloys with additions of Ta and Ta+Ti, respectively, and confirmed later by Wollgarten et al. [60]. With regard to CoCr-base alloys, Berthod et al. [61] recently reported pronounced internal oxidation of Ta and formation of CrTaO_4 in model cast Co–Cr–Ta–C alloys with different Ni contents.

Internal oxidation in AM MAR-M-509 exhibited an approximate parabolic growth, although the extent of the process varied considerably due to the inhomogeneous grain boundary distribution in the alloy (Fig. 2b). Preferential internal oxidation along the grain boundaries was similar to the situation of in situ oxidation of primary carbides discussed previously, as both phenomena involve short-circuit diffusion paths for oxygen represented by matrix grain boundaries [42] and phase interfaces [27], respectively. Comparing the microstructural evolution of the subsurface zone after different exposure times (Figs. 4b and 6b), propagation of the IOZ was accompanied not only by nucleation of new oxide particles, but also by distinct coarsening of the existing precipitates. The latter effect was likely related to mechanisms of Ta/Ti-supply for oxidation with the grain boundaries playing an important role. The Ta/Ti diffusion for formation of initial (Cr, Ti)TaO₄ particles in the AM alloy was mainly governed by the grain boundary transport, as was evident by preferential dissolution of MC carbides along the alloy grain boundaries (Fig. 4d). Considerable amounts of fine MC carbides, however, were still present within the alloy grains. As these precipitates gradually dissolved upon extended exposure, it is possible that a sufficient level of diffusion flux $N_B D_B$ ($B = \text{Ta, Ti}$) could be locally maintained for precipitates coarsening [30].

Formation of internal (Cr, Ti)TaO₄, apart from the oxidation of primary MC carbides, was also found in the cast alloy. Although the number of precipitates

increased with increasing exposure time, the effect remained limited to the scale-alloy interface. It is likely related to the slow dissolution rate of the coarse Ta-rich MC carbides that limits the transport of Ti/Ta available for the oxide formation.

Outer Chromia Scaling and Subscale Depletion Processes

Scale Microstructure

One important experimental observation of the present study is faster oxidation of the cast alloy compared to the AM alloy in the surface areas not apparently affected by the primary carbide oxidation. Despite the very similar chemical composition of the alloy batches (Table 1), the chromia scale on the conventional alloy was generally thicker than that on the AM specimen and exhibited more than 2 times higher growth rate (Fig. 8). Possible reasons for such oxidation behavior require a more detailed microstructural study of the oxide scales.

Morphologies of the oxide scales formed on cast and AM MAR-M-509 after 72 h are illustrated in Figs. 9 and 10, respectively. Coupled EBSD–EDX analysis revealed clear differences in grain structure of the scales. The Cr_2O_3 grown on conventional MAR-M-509 could be characterized by an inhomogeneous grain distribution, although most of the oxide grains exhibited a fine equiaxed morphology. A nearly continuous outer layer of $(\text{Co}, \text{Ni})\text{Cr}_2\text{O}_4$ was also present on the surface in agreement with previous observations in the present study (Fig. 4a, c). On the contrary, the chromia scale on AM MAR-M-509 showed considerably coarser equiaxed oxide grains with finer grains present mainly in the inner part of the scale. Only very minor amounts of outer spinel were observed on the AM alloy.

As Cr_2O_3 possesses very small non-stoichiometry [62], its growth rate is considered to be governed by grain boundary transport rather than lattice diffusion

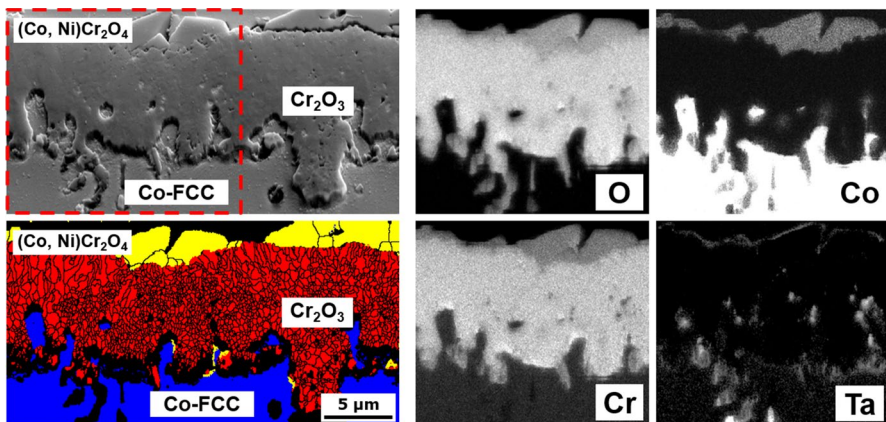


Fig. 9 FSE and EBSD phase color images with EDX element maps of scale grown on cast MAR-M-509 (in distance from areas affected by primary carbides oxidation) after isothermal exposure for 72 h at 1000 °C in air. In the EBSD phase map blue corresponds to the Co-FCC, red to Cr_2O_3 and yellow to (Co, Cr)-spinel

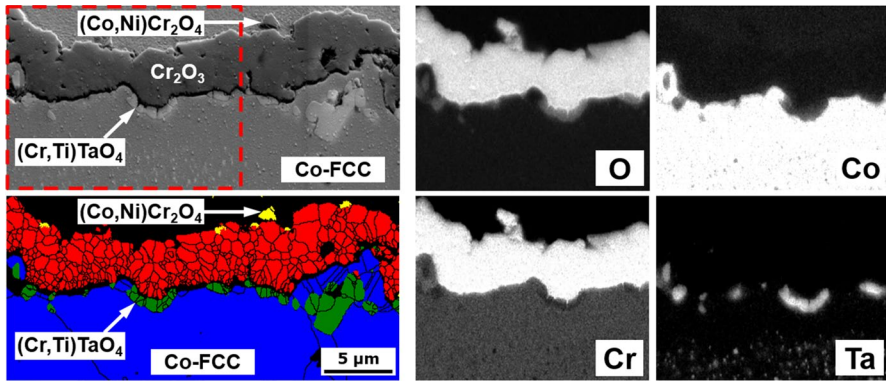


Fig. 10 FSE and EBSD phase color images with EDX element maps of scale grown on AM MAR-M-509 after isothermal exposure for 72 h at 1000 °C in air. In the EBSD phase map blue corresponds to the Co-FCC, red to Cr_2O_3 , green to $(\text{Cr}, \text{Ti})\text{TaO}_4$ and yellow to (Co, Cr) -spinel

[63–65]. High grain boundary density, such as in the fine-grained scale in cast MAR-M-509 (Fig. 9a), promotes the diffusion of oxidizing species leading to a faster Cr_2O_3 growth [66, 67]. There remains, however, the important question of what are the reasons for the different grain structure of chromia scales formed on the cast and AM versions of MAR-M-509.

HAADF STEM images in Fig. 11 compare the oxide scale microstructure in the two investigated versions of MAR-M-509 after 72 h at 1000 °C. The images were obtained in the vicinity of the scale-alloy interface. The chromia scale on the cast alloy featured small grains (note the different magnifications in Fig. 11) with a high number of fine particles present predominantly at the oxide grain-boundaries. Point analysis of the precipitates by EDX indicated a strong enrichment of Cr, W and Co.

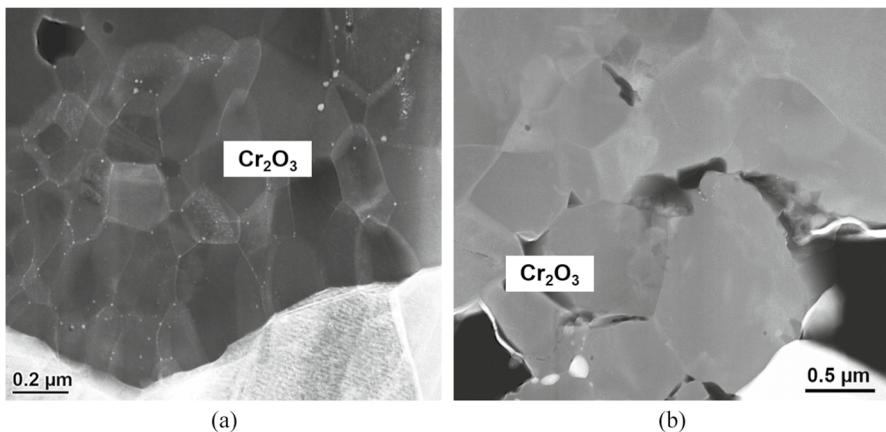


Fig. 11 HAADF STEM images of scales grown on (a) cast and (b) AM MAR-M-509 after isothermal exposure for 72 h at 1000 °C in air. Note different magnification in (a) and (b)

The scale grown on the AM alloy had coarser grains, in agreement with EBSD-data discussed above, and TEM/EDX analysis did not reveal any significant precipitates at the grain-boundaries.

Fine W-rich phase observed at the grain boundaries of Cr_2O_3 on the cast alloy could not be identified by XRD or selective area diffraction pattern TEM analysis due to small volume fraction and, respectively, size of the precipitates. Based on the available data on the Co–W–O [68, 69] and Cr–W–O [70] ternary systems at 1000 °C, formation of CoWO_4 , CrWO_4 and Cr_2WO_6 oxide phases might be considered. CoWO_4 was reported as corrosion product in numerous publications on high-temperature oxidation of W-rich chromia-forming model [71, 72] and commercial [73, 74] Co–Cr–W alloys. Its formation typically occurred when chromia scaling could not be maintained anymore due to critical Cr depletion. Breakdown of the protective scale was followed by rapid formation of a mixed $\text{CoWO}_4 + \text{CoCr}_2\text{O}_4$ scale. With regard to high-temperature oxidation, very limited data are available on CrWO_4 and Cr_2WO_6 oxide phases. According to Jacob [70], CrWO_4 has a limited stability range at 1000 °C (at p_{O_2} level of 10^{-15} to 10^{-11} bar) and decomposes to Cr_2WO_6 at higher oxygen potentials. Unequivocal identification of W-rich precipitates will require the use of advanced characterization techniques such as Atom Probe Tomography in future work.

Interestingly, the mentioned differences in the oxide scale morphology between the cast and AM specimens were not observed after short-term exposure for

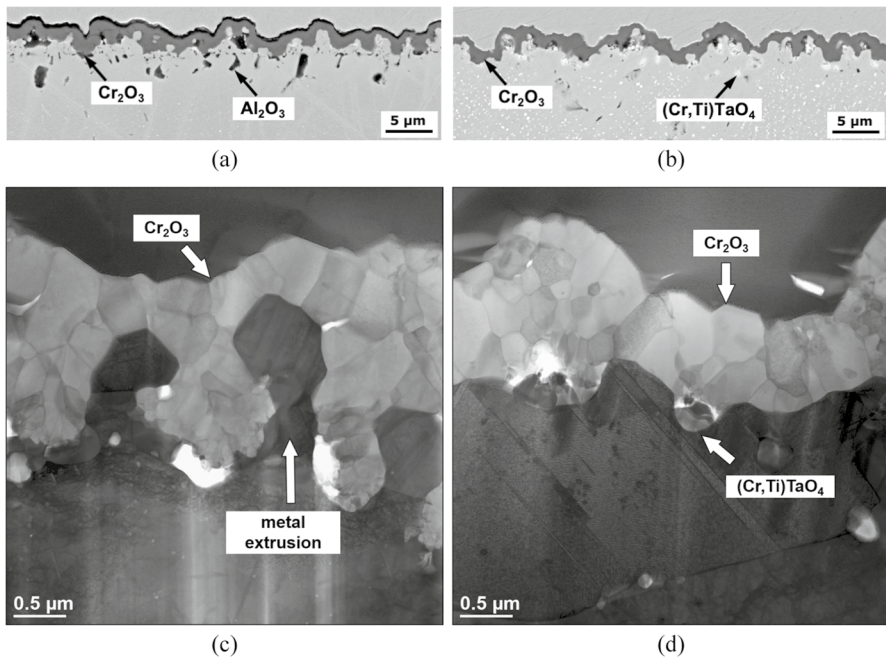


Fig. 12 BSE images and HAADF STEM images of cross-sectioned **a, c** cast and **b, d** AM MAR-M-509 after exposure for 8 h at 1000 °C in air. The analysis of the cast alloy was performed in distance from areas affected by primary carbides oxidation

8 h at 1000 °C, as shown in the BSE and HAADF STEM images in Fig. 12. The oxide scale on the cast alloy was only marginally thicker than on the AM version, $1.2 \pm 0.2 \mu\text{m}$ and $1.0 \pm 0.3 \mu\text{m}$, respectively. No clear indication of outer (Co, Cr)-spinel formation as well as significant scale spallation in the areas not affected by the carbide oxidation was found. In addition, the TEM investigation (Fig. 12b, d) did not show clear differences in grain structure of the chromia scales. No other precipitates at the grain boundaries of the oxide scale were visible. Despite comparable scale thicknesses in the two alloy versions, the EDX-measurements revealed significantly lower Cr levels beneath the oxide scale-alloy interface of the cast alloy (Fig. 13). This experimental observation suggests different Cr transport mechanisms in the cast and the AM alloy and will be discussed in the following section.

The exact reasons for the observed formation of a fine-grain chromia scale on the cast alloy and if this morphology is correlated with the low Cr levels in the subscale region remain unknown. One possible explanation could be attributed to microcracking of the scale due to internal oxidation processes and associated stress generation in the subscale zone [75]. Formation of cracks in the Cr_2O_3 would allow a direct ingress of oxygen to the alloy matrix, which is substantially depleted in Cr in the cast alloy already after short-term exposure (Fig. 13). In this case, healing of the microcracks could be accompanied by formation of the less stable outer Co/Cr-spinel that would further enhance Cr depletion and lead to oxidation of other alloy constituents (e.g., Co, Ni, W) during the crack re-healing. It might be argued that the presence of fine Co/Cr/W-rich particles at the grain-boundaries of Cr_2O_3 could hinder the grain growth during the high-temperature exposure, thus promoting the grain boundary diffusion transport through the scale [66]. In addition, the local volume increase due

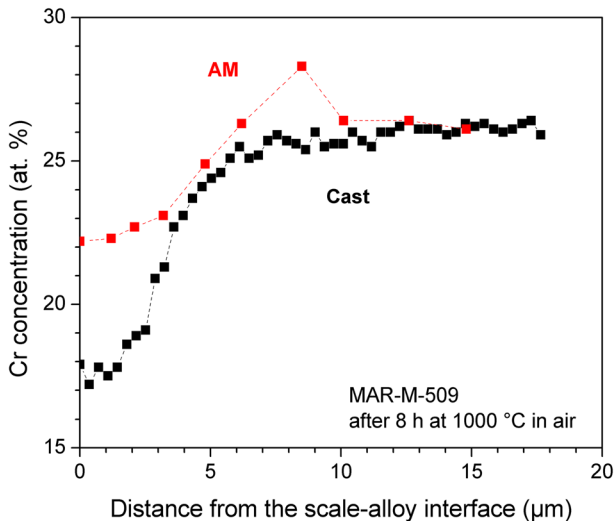


Fig. 13 Cr concentration profiles for cast and AM MAR-M-509 measured by EDX in the alloy matrix after short-term exposure for 8 h at 1000 °C in air. The analysis of the cast alloy was performed in distance from areas affected by primary carbides oxidation. Distinctive peak in the concentration profile of the AM alloy corresponds approximately to the M_{23}C_6 CFZ width

to internal oxide precipitation often results in formation of matrix extrusions into the external oxide scale [76] and its local cracking [75]. Such matrix extrusions become depleted in Cr upon subsequent selective oxidation that could result in formation of less thermodynamically stable transient Co and W-rich oxides prior to re-healing of the cracks.

A similar mechanism of the scale microcracking could also be applied to the AM alloy; however, incorporation of other elements (e.g., Co, Ni, W) during crack re-healing was possibly hindered due to high subscale levels of Cr (Fig. 7b) that ensured rapid formation of Cr_2O_3 .

Differences in Cr Concentration in the Subscale Regions of Cast and AM MAR-M-509

The more pronounced subscale Cr depletion observed in the cast alloy after short-term exposures (in the areas not affected by the carbide oxidation) is at first sight somewhat surprising (Fig. 13). Given the similar scale morphology in the two alloy versions as well as only minor differences in oxide thickness (Fig. 12), a comparable Cr distribution beneath the oxide scale would be expected.

According to Wagner's treatment of selective oxidation [77], the interface concentration of the scale forming element in a binary alloy N_B^i depends on its initial concentration N_B^0 , diffusion coefficient in the alloy matrix D_B and metal recession rate k_c , which is related to the parabolic rate constant through the Pilling-Bedworth ratio [78]

$$N_B^i = N_B^0 - \left(\frac{\pi k_c}{2D_B} \right)^{1/2} \quad (4)$$

The resulting depletion profiles during continuous oxidation are thus strongly related to the k_c/D_B ratio. A high interface concentration of the scale forming element may result at low values of the ratio k_c/D_B , i.e., when the oxidation rate is small and/or the diffusion in the alloy matrix is rapid [79]. Such a situation is often observed during oxidation of high Cr ferritic steels, where fast diffusion of Cr in Fe-BCC matrix results in nearly flat concentration profiles beneath the oxide scale [75, 80]. During short-term exposure, cast and AM MAR-M-509 exhibited comparable growth rates of the chromia scale (Fig. 12). In this case, k_c can be assumed to be virtually equal, whereas D_{Cr} should then be considerably higher in the AM alloy. While the diffusion coefficients of species in the Co-matrix are not likely to be significantly different in the studied materials due to the similar chemical composition (Table 1), the alloy microstructure as well as the morphology of the Cr-rich precipitate phases (Fig. 2) can have a strong effect on the Cr transport toward the oxidizing surface.

A significant contribution to the diffusional flux of Cr could be provided by the oxidation-induced dissolution of fine Cr-rich M_{23}C_6 carbides that were evenly distributed along the grain-boundaries of the AM alloy (Fig. 2b). Such a morphology of the Cr-rich precipitates is known to be beneficial in establishing and maintaining the external oxide scale, as fine precipitates dissolve rapidly in the subscale zone and supply Cr for the oxide formation [81, 82]. Formation of the carbide free zone was

visible in the AM alloy already after oxidation for 8 h. In the case of the cast alloy, the dissolution of coarse Cr-rich carbides was not likely to provide a high Cr flux during the initial stages of exposure due to their relatively slow dissolution as well as irregular distribution in the alloy matrix. The Cr supply was thus limited to Cr diffusion present in the Co-matrix.

In addition, the fine-grained microstructure of the AM alloy (Fig. 2b) is likely to promote Cr diffusion along the grain boundaries [65], similar to the effect reported for commercial Fe–Cr–Ni alloys [83, 84] and wrought Ni-base alloys [85]. Considering the relatively low Cr diffusion coefficient in Co, which is about one order of magnitude lower than that in Ni [16], Cr transport along the alloy grain-boundaries must be playing an important role in securing high levels of Cr in the subscale zone.

Conclusions

The present study focused on the oxidation behavior of two versions of the cobalt-base turbine blade and vane alloy MAR-M-509—conventionally cast and produced by Selective Laser Melting. Both alloy batches had similar chemical compositions (except for the amount of Al as a minor alloying element), but possessed completely different microstructures that appeared to have a tremendous effect on the oxidation kinetics.

High-temperature oxidation of the cast alloy was significantly affected by coarse primary Ta/Ti-rich carbides present in the microstructure. When located close to the specimen surface, these precipitates underwent rapid oxidation during exposure resulting in formation of thick oxide nodules of mixed composition. The process was accompanied by local volume increase and development of pores and cracks in the adjacent areas of the Cr₂O₃ scale, thus promoting its spallation. Moreover, a higher Al content in the cast alloy, the presence of microstructural defects in the oxide scale and its poor adherence allowed ingress of nitrogen to the metal surface causing internal nitridation of Al.

In contrast to the cast alloy, AM MAR-M-509 exhibited substantially slower oxidation with about one order of magnitude lower oxidation rate, as revealed by TG-analysis at 1000 °C. This behavior was related to the fundamentally different microstructure revealing fine carbide precipitates at the grain boundaries and in the grain interior. Instead of direct oxidation upon high-temperature exposure, fine carbides (mainly of Ta/Ti-rich MC-type) were found to dissolve in the subsurface region to form internal Ta/Ti-rich oxides beneath the external chromia, which was more homogeneous and dense than that on the cast alloy. Internal nitridation processes were not observed in the AM alloy due to more gas-tight and better adherent oxide scale and lower alloy Al content.

Another difference in the oxidation behavior of the cast and the AM alloy was related to the extent of subscale depletion processes. Low Cr concentration levels beneath the oxide scale were observed in the cast alloy already after short-term oxidation, whereas Cr concentration profiles showed only minor depletion in the AM samples even after longer exposure times. The effect was correlated with the rapid dissolution of fine Cr-rich carbides in the subscale zone that provided a high Cr flux

toward the oxidizing surface. An additional significant contribution to maintaining a high Cr content at the scale-alloy interface was attributed to the fine-grained microstructure of the AM alloy that promoted Cr diffusion along the grain-boundaries.

Apart from the oxidation processes directly related to the differences in the alloy microstructure and the morphology of strengthening precipitates, the cast alloy showed faster growth of Cr_2O_3 compared to the AM version and featured formation of the outer Co/Cr-spinel, even in the areas not directly affected by oxidation of primary carbides. Based on the detailed microstructural studies using SEM-EBSD and TEM, this effect was attributed to the fine-grained morphology of the chromia scale resulting in enhanced mass transport. This morphology of the scale is proposed to originate from incorporation of Co and W into the Cr_2O_3 and their segregation at the grain-boundaries in the form of small oxide precipitates, thus hindering the grain growth of the oxide. Formation of less stable oxide phases in the scale on the cast alloy could be related to microcracking of the Cr_2O_3 induced by internal oxidation processes and associated formation of matrix extrusions into the scale that provided direct access of oxygen to the Cr-depleted alloy matrix. Although a similar mechanism could operate in the AM alloy, incorporation of other elements (e.g., Co, Ni, W) during crack re-healing could be suppressed by the above-mentioned high sub-scale concentration of Cr ensured by rapid dissolution of fine Cr-rich carbides as well as pronounced GB diffusion in the alloy matrix.

Acknowledgements The authors are grateful to Dr. R. Herzog and Mr. M. Ernsberger from MAN Energy Solutions SE for providing Co-base materials for the present study. Following colleagues in the Institute for Energy and Climate Research of the Forschungszentrum Jülich GmbH are greatly acknowledged: Mr. H. Cosler and Ms. A. Kick for carrying out the high-temperature exposures, Dr. E. Wessel and Dr. D. Grüner for SEM/EDX/EBS and TEM analyses, and Mr. M. Ziegner for XRD analyses.

Author contributions TG: conceptualization, investigation, data curation, writing—original draft. RP: conceptualization, supervision, writing—review and editing. WJQ: writing—review and editing, funding acquisition. DN: conceptualization, supervision, writing—review and editing, funding acquisition.

Funding Open Access funding enabled and organized by Projekt DEAL. The study was funded by the Forschungszentrum Jülich GmbH (internal funding).

Availability of data and materials Neither supplementary material nor related files were submitted for the review of the manuscript.

Declarations

Conflict of interest The authors declare that they have no conflict of interest.

Ethics approval and consent to participate Not applicable.

Consent for publication All authors gave explicit consent to submit the study.

Open Access This article is licensed under a Creative Commons Attribution 4.0 International License, which permits use, sharing, adaptation, distribution and reproduction in any medium or format, as long as you give appropriate credit to the original author(s) and the source, provide a link to the Creative Commons licence, and indicate if changes were made. The images or other third party material in this article are included in the article's Creative Commons licence, unless indicated otherwise in a credit line to the material. If material is not included in the article's Creative Commons licence and your intended use is not permitted by statutory regulation or exceeds the permitted use, you will need to obtain permission

directly from the copyright holder. To view a copy of this licence, visit <http://creativecommons.org/licenses/by/4.0/>.

References

1. J. R. Davis, *ASM Specialty Handbook: Heat Resistant Materials*, (ASM International, Novelty, 1997).
2. M. G. Fahrman, V. P. Deodeshmukh, and S. K. Srivastava, *Journal of Engineering for Gas Turbines and Power - ASME* **139**, 7 (2017).
3. G. Y. Lai, *High-Temperature Corrosion and Materials Applications*, (ASM International, Novelty, 2007).
4. M. D. Rowe, V. R. Ishwar, and D. L. Klarstrom, *Journal of Engineering for Gas Turbines and Power - ASME* **128**, 354 (2006).
5. C. T. Sims, *Journal of Metals* **21**, 27 (1969).
6. C. Berger and H. W. Gruenling, in *Stationaere Gasturbinen*, eds. C. Lechner and J. Seume (Springer, 2010), p. 785.
7. Klarstrom DL. In: *Heat Treating of Nonferrous Alloys*, eds. G. E. Totten and D. S. MacKenzie (ASM International, 2016), p. 625.
8. C. A. Barrett, In: *Environmental Degradation of Engineering Materials*, eds. M. R. Louthan and R. P. McNitt (1977), p. 319.
9. A. Preece and G. Lucas, *Journal of the Institute of Metals* **81**, 219 (1952).
10. P. K. Kofstad and A. Z. Hed, *Journal of the Electrochemical Society* **116**, 1542 (1969).
11. G. C. Wood, I. G. Wright, T. Hodgkiess, and D. P. Whittle, *Materials and Corrosion* **21**, 900 (1970).
12. C. A. Phalnikar, E. B. Evans, and W. M. Baldwin, *Journal of the Electrochemical Society* **103**, 429 (1956).
13. I. G. Wright and G. C. Wood, *Oxidation of Metals* **11**, 163 (1977).
14. B. Chattopadhyay and G. C. Wood, *Oxidation of Metals* **2**, 373 (1970).
15. D. L. Douglass and J. S. Armijo, *Oxidation of Metals* **3**, 185 (1971).
16. A. Green, D. P. Whittle, J. Stringer, and N. Swindell, *Scripta Metallurgica* **7**, 1079 (1973).
17. S. S. Babu, N. Raghavan, J. Raplee, et al., *Metallurgical and Materials Transactions A* **49A**, 3764 (2018).
18. B. Blakey-Milner, P. Gradl, G. Snedden, et al., *Materials & Design* **209**, 110008 (2021).
19. A. Seidel, T. Finaske, A. Straubel, et al., *Metallurgical and Materials Transactions A* **49A**, 3812 (2018).
20. M. Cloots, K. Kunze, P. J. Uggowitzer, and K. Wegener, *Materials Science and Engineering: A* **658**, 68 (2016).
21. P. Kanagarajah, F. Brenne, T. Niendorf, and H. J. Maier, *Materials Science and Engineering: A* **588**, 188 (2013).
22. K. Kunze, T. Etter, J. Grässlin, and V. Shklover, *Materials Science and Engineering: A* **620**, 213 (2015).
23. T. Sanviemvongsak, D. Monceau, and B. Macquaire, *Corrosion Science* **141**, 127 (2018).
24. M. Romedenne, R. Pillai, M. Kirka, and S. Dryepondt, *Corrosion Science* **171**, 108647 (2020).
25. A. Chyrkin, K. O. Gunduz, I. Fedorova, et al., *Corrosion Science* **205**, 110382 (2022).
26. M. Romedenne, P. Stack, R. Pillai, and S. Dryepondt, *JOM* **74**, 1 (2022).
27. A. M. Beltran, C. T. Sims, and N. T. Wagenheim, *JOM* **21**, 39 (1969).
28. J. Reuchet and L. Remy, *Materials Science and Engineering*. **58**, 19 (1983).
29. J. R. Lane and N. J. Grant, *Transactions of the American Society for Metals* **44**, 113 (1952).
30. A. K. Jena and M. C. Chaturvedi, *Journal of Materials Science* **19**, 3121 (1984).
31. D. N. Astrov, N. A. Kryukova, R. B. Zorin, et al., *Soviet Physics Crystallography* **17**, 1017 (1973).
32. W. Ruedorff and H. Luginsland, *Journal of Inorganic and General Chemistry* **334**, 125 (1964).
33. A. Petersen and H. Mueller-Buschbaum, *Journal of Inorganic and General Chemistry* **609**, 51 (1992).

34. W. J. Quadackers, D. Naumenko, E. Wessel, V. Kochubey, and L. Singheiser, *Oxidation of Metals* **61**, 17 (2004).
35. S. A. Eliziario, J. M. de Andrade, S. J. G. Lima, et al., *Materials Chemistry and Physics* **129**, 619 (2011).
36. P. J. Ennis, W. J. Quadackers, and H. Schuster, *Materials Science and Technology* **8**, 78 (1992).
37. A. Chyrkin, R. Pillai, H. Ackermann, et al., *Corrosion Science* **96**, 32 (2015).
38. M. Reger and L. Remy, *Metallurgical Transactions a-Physical Metallurgy and Materials Science* **19**, 2259 (1988).
39. J. Reuchet and L. Remy, *Materials Science and Engineering* **58**, 33 (1983).
40. N. Belen, P. Tomaszewicz, and D. J. Young, *Oxidation of Metals* **22**, 227 (1984).
41. P. Becker, M. Panasko, and D. J. Young, *Oxidation of Metals* **64**, 281 (2005).
42. D. P. Whittle, Y. Shida, G. C. Wood, F. H. Stott, and B. D. Bastow, *Philosophical Magazine A* **46**, 931 (1982).
43. F. H. Stott, G. C. Wood, D. P. Whittle, B. D. Bastow, Y. Shida, and A. Martinezvillafane, *Solid State Ionics* **12**, 365 (1984).
44. I. C. Chen and D. L. Douglass, *Oxidation of Metals* **38**, 189 (1992).
45. U. Krupp, in *Shreir's Corrosion*, eds. B. Cottis, M. Graham, R. Lindsay, et al. (Elsevier, Oxford, 2010), p. 304.
46. G. Y. Lai, in *ASM 1993 Materials Congress Materials Week*, eds. V. P. Swaminathan and N. S. Cheruvu (ASM International, 1993), p. 113.
47. C. A. Snavely and C. L. Faust, *Journal of the Electrochemical Society* **97**, 99 (1950).
48. G. R. Wilms and T. W. Rea, *Journal of the Less-Common Metals* **3**, 234 (1961).
49. U. Krupp, S. Y. Chang, A. Schimke, H. J. Christ, *EFC Workshop on Lifetime Modelling of High Temperature Corrosion Processes* (2001), p. 148.
50. J. Litz, A. Rahmel, M. Schorr, and J. Weiss, *Oxidation of Metals* **32**, 167 (1989).
51. U. Krupp and H.-J. Christ, *Metallurgical and Materials Transactions A* **31**, 47 (2000).
52. S. Han and D. J. Young, *Oxidation of Metals* **55**, 223 (2001).
53. H. J. Christ, S. Y. Chang, and U. Krupp, *Materials and Corrosion* **54**, 887 (2003).
54. J. L. Meijering, in *Advances in Materials Research*. ed. H. Herman (Wiley-Interscience, New York, 1971).
55. D. L. Douglass, *JOM* **43**, 74 (1991).
56. D. L. Douglass, *Oxidation of Metals* **44**, 81 (1995).
57. D. J. Young, in *High Temperature Oxidation and Corrosion of Metals*, 2nd ed, ed. D. J. Young (Elsevier, 2016), p. 261.
58. A. Jalowicka, W. Nowak, D. Naumenko, L. Singheiser, and W. J. Quadackers, *Materials and Corrosion-Werkstoffe Und Korrosion* **65**, 178 (2014).
59. W. J. Nowak, B. Wierzba, and J. Sieniawski, *High Temperature Materials and Processes* **37**, 801 (2018).
60. K. Wollgarten, T. Galiullin, W. J. Nowak, W. J. Quadackers, and D. Naumenko, *Corrosion Science* **173**, 108774 (2020).
61. P. Berthod and J. P. Gomis, *Corrosion Engineering Science and Technology* **55**, 118 (2020).
62. P. Kofstad, *Oxidation of Metals* **44**, 3 (1995).
63. A. C. S. Sabioni, A. M. Huntz, F. Millot, and C. Monty, *Philosophical Magazine A* **66**, 351 (1992).
64. A. C. S. Sabioni, A. M. Huntz, F. Millot, and C. Monty, *Philosophical Magazine A* **66**, 361 (1992).
65. D. Caplan, M. J. Graham, and M. Cohen, *Journal of the Electrochemical Society* **119**, 1205 (1972).
66. J. Zurek, D. J. Young, E. Essuman, et al., *Materials Science and Engineering A* **477**, 259 (2008).
67. D. Caplan and G. I. Sproule, *Oxidation of Metals* **9**, 459 (1975).
68. A. Trumm, *Neues Jahrbuch für Mineralogie* **6**, 267 (1979).
69. G. J. French and F. R. Sale, *Journal of Materials Science* **20**, 1291 (1985).
70. K. T. Jacob, *Journal of Materials Science* **15**, 2167 (1980).
71. S. Espevik, R. A. Rapp, P. L. Daniel, and J. P. Hirth, *Oxidation of Metals* **20**, 37 (1983).
72. M. E. Eldahshan, D. P. Whittle, and J. Stringer, *Corrosion Science* **16**, 77 (1976).
73. J. S. Wolf and G. D. Sandroek, *Some Observations Concerning the Oxidation of the Cobalt-Base Superalloy L-605 (Hs-25)* (Lewis Research Center, National Aeronautics and Space Administration, 1968).

74. C. E. Lowell and D. L. Deadmore, *Oxidation of Metals* **7**, 55 (1973).
75. P. Huczowski, S. Ertl, J. Piron-Abellan, et al., *Materials at High Temperatures* **22**, 253 (2005).
76. H. C. Yi, S. W. Guan, W. W. Smeltzer, and A. Petric, *Acta Metallurgica Et Materialia* **42**, 981 (1994).
77. C. Wagner, *Journal of the Electrochemical Society* **99**, 369 (1952).
78. N. B. Pilling and R. E. Bedworth, *Journal of the Institute of Metals* **29**, 529 (1923).
79. D. J. Young, A. Chyrkin, and W. J. Quadackers, *Oxidation of Metals* **77**, 253 (2012).
80. P. Huczowski, N. Christiansen, V. Shemet, J. Piron-Abellan, L. Singheiser, and W. J. Quadackers, *Materials and Corrosion* **55**, 825 (2004).
81. G. Wang, B. Gleeson, and D. L. Douglass, *Oxidation of Metals* **35**, 333 (1991).
82. R. N. Durham, B. Gleeson, and D. J. Young, *Oxidation of Metals* **50**, 139 (1998).
83. V. B. Trindade, U. Krupp, P. E. G. Wagenhuber, and H. J. Christ, *Materials and Corrosion* **56**, 785 (2005).
84. N. Otsuka, Y. Shida, and H. Fujikawa, *Oxidation of Metals* **32**, 13 (1989).
85. F. Abe, H. Araki, H. Yoshida, M. Okada, and R. Watanabe, *Corrosion Science* **21**, 819 (1981).

Publisher's Note Springer Nature remains neutral with regard to jurisdictional claims in published maps and institutional affiliations.